Bio-Design and Manufacturing
https://doi.org/10.1631/bdm.2300365

RESEARCH ARTICLE

Optimization-based conformal path planning for in situ bioprinting during complex skin defect repair

Wenxiang Zhao[1,2] · Chuxiong Hu[1,2] · Yunan Wang[1,2] · Shize Lin[1,2] · Ze Wang[1,2] · Tao Xu[3]

Received: 19 December 2023 / Accepted: 24 October 2024

Abstract

The global demand for effective skin injury treatments has prompted exploration of tissue engineering solutions. While three-dimensional (3D) bioprinting has shown promise, challenges persist with respect to achieving timely and compatible solutions to treat diverse skin injuries. In situ bioprinting has emerged as a key new technology, since it reduces risks during the implantation of printed scaffolds and demonstrates superior therapeutic effects. However, maintaining printing fidelity during in situ bioprinting remains a critical challenge, particularly with respect to model layering and path planning. This study proposes a novel optimization-based conformal path planning strategy for in situ bioprinting-based repair of complex skin injuries. This strategy employs constrained optimization to identify optimal waypoints on a point cloud-approximated curved surface, thereby ensuring a high degree of similarity between predesigned planar and surface-mapped 3D paths. Furthermore, this method is applicable for skin wound treatments, since it generates 3D-equidistant zigzag curves along surface tangents and enables multi-layer conformal path planning to facilitate treatment of volumetric injuries. Furthermore, the proposed algorithm was found to be a feasible and effective treatment in a murine back injury model as well as in other complex models, thereby showcasing its potential to guide in situ bioprinting, enhance bioprinting fidelity, and facilitate improvement of clinical outcomes.

✉ Chuxiong Hu
cxhu@tsinghua.edu.cn

[1] Department of Mechanical Engineering, Tsinghua University, Beijing 100084, China

[2] Beijing Key Laboratory of Precision and Ultra-Precision Manufacturing Equipment and Control, Tsinghua University, Beijing 100084, China

[3] Center for Bio-intelligent Manufacturing and Living Matter Bioprinting, Research Institute of Tsinghua University in Shenzhen, Tsinghua University, Shenzhen 518057, China

Graphic abstract

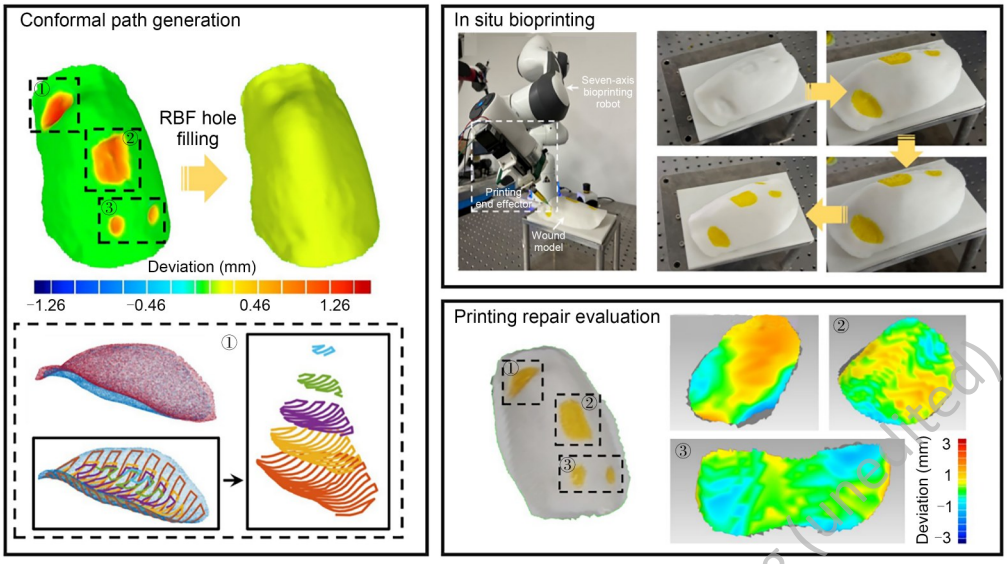

Keywords In situ bioprinting · Path planning · Robot control · Skin injury repair

1 Introduction

The skin, the largest organ in the human body, serves as a protective barrier against external elements [1]. Globally, the high prevalence of skin injuries such as burns and chronic ulcers has created significant demand for effective treatments [2, 3]. While tissue engineering, including three-dimensional (3D) bioprinting technology, has shown both efficacy and potential [4, 5], practical challenges arise due to diverse skin injury characteristics, including injury shape, depth, and location [6, 7]. Tissue-engineered skin constructed using conventional benchtop bioprinters can struggle to achieve an ideal match with defect sites and may present additional risks of contamination or tissue damage during implantation [8]. In response, in situ bioprinting, a process performed in a clinical setting in which a bioink is directly deposited inside a defect to create a living tissue, has emerged as a new way to address these challenges [9]. In general, this in situ approach integrates a traditional two-step "print-implant" strategy into a single step, thereby reducing potential risks during implantation and decreasing donor waiting time for tissue maturation, which is an important limitation of conventional bioprinting. Moreover, in situ techniques have demonstrated superior therapeutic effects with respect to soft tissue repair in animal experimental validation studies [10–15].

One critical objective of in situ bioprinting is maintaining printing fidelity, which is closely related to model layering and path planning during the pre-printing stage [8]. Unlike conventional bioprinting, which is based on planar layering and printing on a flat surface, the substrate of in situ bioprinting is the defect itself, and this can have complex topographical features. Proceeding with planar layering not only leads to interruptions in the printing path but can also generate a stair-step effect, thereby inducing nonnegligible fabrication errors [16 – 18]. More importantly, this simplified layering pattern is not conductive to constructing tissue scaffolds that can directionally interface with native tissues. Moreover, Wang et al. suggested that this may not be suitable for tissue-specific slicing strategies required to treat composite tissue injuries [19]. Therefore, the conformal layering method, in which each layer bears a similar profile to the topography of the skin defect, holds significant implications for in situ bioprinting.

Currently, research on conformal slicing in in situ bioprinting applications remains limited, which has prompted us to focus on layering studies for multi-axis 3D printing. For instance, Mitropoulou et al., inspired by key-framing techniques used in animation, generated non-planar layers through smooth interpolation based on predefined curves and shape constraints corresponding to the designed structure [20]. This approach has proven to be effective for thin-shell and bifurcating structures [21]. To improve slicing efficiency, a protocol was developed by Fortunato that involved the extraction of the outer surface structure for the starting and ending layers, while adopting traditional planar slicing schemes for intermediate (i.e., unseen) portions [22]. This hybrid approach ensures shape fidelity while reducing slicing complexity. Yigit and Lazoglu reported another method that featured directly

integrated slicing and path planning, as well as a spiral slicing method to eliminate interlayer seam defects [23, 24]. These studies in architecture and manufacturing [25] collectively highlight the necessity of conformal layering for improving shape fidelity, eliminating support structures, and enhancing efficiency.

In addition to model layering, conformality in path planning, i.e., the process specifying the optimal compliance and similarity between the generated spatial path and the corresponding 3D surfaces [26], can also contribute to printing fidelity. For determining the path printed on 3D surfaces, current research typically relies on a surface projection plane to plan a two-dimensional (2D) path, and then extends this path into a 3D space [27–29]. For example, Lian et al. designed a planar path based on 2D information extracted from a scanned point cloud and subsequently used a lookup table to identify the corresponding 3D waypoints [30]. Similarly, Zhou and colleagues used a similar approach for generating spatial paths for printing on the surfaces of living tissues [31]. Rodriguez-Padilla et al. proposed a method for generating curved printing paths by projecting discrete planar waypoints onto stereolithography (STL) models and then intersecting each waypoint with triangles produced by the STL models; this method was able to achieve better conformality [32]. Overall, these methods simply add an extra dimension to 2D waypoints and neglect the conformality of spatial paths with the surfaces. For instance, issues arising from the Euclidean distance between waypoints can result in varying internals of equidistant curves in the plane even after mapping to three dimensions. Moreover, right angles in the plane, when projected, transform into sharp angles and abrupt turns. In a printing scenario, these problems can lead to defects such as over- or underfilling, and therefore pose challenges for the position and velocity control of the printing end effector [28, 33]. Moreover, obstacles remain with respect to conducting in situ bioprinting to close wounds within a desired precision, especially for skin wounds with unpredictable surfaces and complex borders. Some research in robotic trajectory planning [34, 35] has focused on optimization methods capable of generating optimal maps for planar paths. However, these methods involve surface parameterization steps and therefore have limited applicability.

In this paper, we propose a novel optimization-based conformal path planning strategy for in situ bioprinting during repair of complex skin injuries that avoids many of these limitations. This strategy is based on the formulation of an objective function and employs constrained optimization to find optimal waypoints on a point cloud-approximated curved surface, thereby ensuring the highest similarity in shape and angle between the predesigned planar path and the surface-mapped 3D path. When used for skin wound treatment applications, this strategy can be directly applied to the point cloud that defines a specific wound, and may thereby enable the instant generation of 3D equidistant zigzag curves along the surface tangent without requiring the assistance of 2D paths. Furthermore, multi-layer conformal path planning can be achieved in combination with the conformal layering methods for complex volumetric injuries. This optimization-based method involves the abstract fitting of a region of interest (ROI) of the point cloud, and does not require mathematical expressions of the substrate surface, a feature that makes this procedure suitable for irregular surfaces such as skin defects. Finally, several different conformal paths are generated on various surfaces to demonstrate the universality of the proposed strategy. Meanwhile, multi-layer conformal paths were designed for wound filling on a murine back injury model, and in situ bioprinting was performed using a developed multi-depth of field (DoF) bioprinter.

2 Methods

2.1 Optimization-based conformal path planning

The core of the proposed path planning algorithm can be summarized as discretizing a predefined path and then mapping scattered points onto its surface while maintaining its shape and angular structure. This section will primarily introduce the principles and processes involved in optimization-based conformal path generation, including parameter definition and the construction of optimization functions for shape and angle preservation. In addition, planar paths and 3D models are also established for method verification.

2.1.1 Parameter definition

We consider a surface $S(x,y,z) \subset \mathbb{R}^3$, a planar path $P(u, v) \subset \mathbb{R}^2$, and a mapping relationship $r_s{:}\mathbb{R}^2 \rightarrow \mathbb{R}^3$ such that $P_0(u_0,v_0)$ is the initial point on path P and that v_0 denotes the start direction of P. In this context, x, y, and z represent the 3D coordinates of a point within the surface S, and similarly, u and v denote the coordinate values on the planar path P. To obtain the global mapping of P onto S, a stepwise search is conducted on P using a step size defined as stp, where the angle between stepping points is defined as θ. For the initial point, θ is defined as the angle between v_0 and the x-direction of the coordinate axis. Moreover, l and w represent the length and width of the ROI in the point cloud that defines the surface S, respectively; these values are used when optimizing the spatial stepping points on S. These parameters can be clearly identified in Fig. 1.

2.1.2 Conformal mapping with shape preservation

Based on $P_0(u_0,v_0)$, v_0, and stp, a portion of the point cloud can be filtered as the ROI, which is typically a narrow

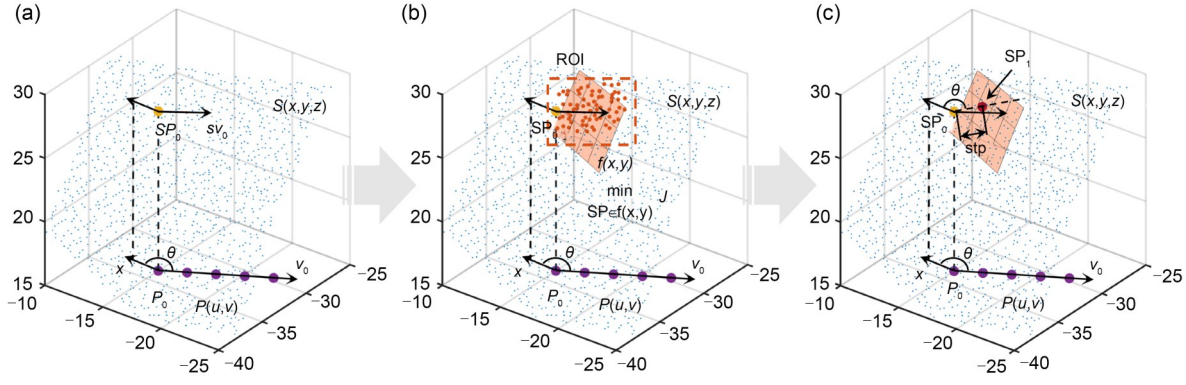

Fig. 1 Illustrative flowchart of optimization-based conformal path generation. (a) Given the planar path P and the spatial point cloud S, we map P conformally onto S. P_0 and SP_0 represent the initial points, while v_0 and sv_0 represent the initial directions. (b) We select the region of interest (ROI) on S and fit a plane f based on points within the ROI. (c) Finally, we search for the next point SP_1 on the fitted plane f, adhering to the constraints of shape and angle preservation

rectangular region starting from $P_0(u_0, v_0)$ in the direction v_0. Empirically, setting l as 1 times stp and w as 0.5 times stp enables accurate target point retrieval at a relatively small computational cost. Next, we fit the ROI using a quadratic surface, expressed as follows:

$$\begin{bmatrix} x_1^2 & y_1^2 & x_1y_1 & x_1 & y_1 & 1 \\ \vdots & \vdots & \vdots & \vdots & \vdots & \vdots \\ x_m^2 & y_m^2 & x_my_m & x_m & y_m & 1 \end{bmatrix} \begin{bmatrix} a_{20} \\ a_{02} \\ a_{11} \\ a_{10} \\ a_{01} \\ a_{00} \end{bmatrix} = \begin{bmatrix} f(x_1, y_1) \\ \vdots \\ f(x_m, y_m) \end{bmatrix} \quad (1)$$

Here, a represents the coefficients of surface expression and m represents the number of points within the ROI. Commonly, m points are sufficient to support surface fitting based on the least squares method, and the equation defined by $f(x, y)$ can be acquired.

An essential requirement for shape preservation is to identify a mapped stepping point on surface S that minimizes the deviation between the geodesic path distance and the region defined by stp [34]. Hence, the optimization problem can be formulated as follows:

$$\begin{aligned} &\underset{\mathrm{SP}}{\text{minimize}}\ J = \sum_{i=1}^{L} \left| \left\| \mathrm{SP}_i - \mathrm{SP}_{i-1} \right\| - \mathrm{stp} \right| \\ &\text{subject to } \mathrm{SP} \in f(x, y) \end{aligned} \quad (2)$$

Here, L represents the number of segments into which the path P is divided by stp, and SP denotes the mapping of path P onto surface S.

To solve the minimization problem, we employed an interior-point optimization algorithm [36] for constrained iteration. This was accomplished using the fmincon function implemented in MATLAB. Furthermore, we note that numerical optimization can be highly sensitive to initial values, and therefore choosing an appropriate initial guess plays a crucial role in reducing the number of iterations and in avoiding numerical divergence, especially when the convexity of the objective function J is not emphasized. Thus, the point in the ROI that is closest to the initial point in terms of distance to stp is selected as the initial estimate, and this value demonstrated rapid and accurate convergence in subsequent simulations and trials.

2.1.3 Conformal mapping with shape and angle preservation

Maximizing shape preservation and minimizing angular distortion can help to maintain the structural and geometric similarity of the spatial path to the original path P in 2D. As in Eq. (2), an optimization function with the objective of minimizing angular distortion can be written as follows:

$$\begin{aligned} &\underset{\mathrm{SP}}{\text{minimize}}\ J = \\ &\sum_{i=1}^{L-1} \left| \frac{(\mathrm{SP}_{i-1} - \mathrm{SP}_i) \cdot (\mathrm{SP}_{i+1} - \mathrm{SP}_i)}{\left\| \mathrm{SP}_{i-1} - \mathrm{SP}_i \right\| \left\| \mathrm{SP}_{i+1} - \mathrm{SP}_i \right\|} - \cos\theta \right| \\ &\text{subject to } \mathrm{SP} \in f(x, y) \end{aligned} \quad (3)$$

However, on the irregular surface S, simultaneously optimizing for distance and angle as objectives is contradictory and poses challenges with respect to diversity and convergence during implementation. Hence, inspired by cosine similarity and Euclidean distance procedures used in information retrieval [37], we note that Eqs. (2) and (3) can be unified into a normalized model as shown below.

$$\begin{aligned} &\underset{\mathrm{SP}}{\text{minimize}}\ J = \frac{\sum_{i=1}^{L} \frac{\left| \left\| \mathrm{SP}_i - \mathrm{SP}_{i-1} \right\| - \mathrm{stp} \right|}{\mathrm{stp}}}{L} + \\ &\frac{\sum_{i=1}^{L-1} \left| \frac{(\mathrm{SP}_{i-1} - \mathrm{SP}_i) \cdot (\mathrm{SP}_{i+1} - \mathrm{SP}_i)}{\left\| \mathrm{SP}_{i-1} - \mathrm{SP}_i \right\| \left\| \mathrm{SP}_{i+1} - \mathrm{SP}_i \right\|} - \cos\theta \right|}{2(L-1)} \\ &\text{subject to } \mathrm{SP} \in f(x, y) \end{aligned} \quad (4)$$

The specific derivation of this equation can be found in a previously published study [38]. In this model, the parts representing distance and angle errors are separately normalized, ensuring that their values remain within the range (0,1). This normalization makes the optimization processes of both parts equivalent with respect to their impact on the objective function. Moreover, the same interior-point optimization algorithm and initial estimation are used for this function, and do not increase the computational complexity. Equation (4) is therefore used as the objective function in the rest of this work.

2.1.4 Examples of conformal path generation on 3D surfaces

Next, to validate our fitting and optimization algorithms, we employed three surfaces as mapping substrates: a semi-ellipsoid with axes ratios of 11:10:9, a mathematical surface represented by $z=0.5\times\cos(x+\cos(y))$, and a folded origami protrusion structure in the shape of a hexagram. On each of these surfaces, various curves were mapped, including zigzag paths with varying intervals and orientations, square spiral patterns, and simplified Chinese knot patterns. For each mapping instance, the initial point on the surface is first manually determined. Then, based on stp, the corresponding waypoints on the surface are determined using the optimization function, Eq. (4). Within the optimization function J, the traversal step size of the 2D patterns is the only variable. Therefore, to determine a suitable stp, we considered the portion representing the distance measurement J_d and the part representing the angle similarity J_a as well as the computation time required for the optimization calculation. All calculations here were performed on a personal computer equipped with an Intel i7 processor and 8 GB random access memory.

2.2 Conformal path generation strategy for wound repair

Due to the strict conformal constraints of the proposed method, the coverage area can change when mapping a predefined planar path onto a curved surface. Unfortunately, this is not conducive to effective wound repair. As illustrated in Fig. 2, when in situ bioprinting is carried out on a curved surface to fill an open wound (i.e., the area represented by red points), even though the 2D path planed in the projection plane is faithfully mapped onto the surface in such a way that it avoids printing defects, the generated conformal path may be unable to completely cover the injury. Therefore, improvements to the optimization-based path generation method are required for wound repair scenarios. This includes the directly generation of conformal paths pointwisely on the surface without relying on predefined planar paths as well as the development of a method for the conformal layering and multi-layer path generation for filling volumetric wounds.

2.2.1 Single-layer paths for wound coverage

Improvement of optimization-based path planning methods can occur via directly generating a conformal single-layer printing path on the wound surface without relying on a predesigned planar path. This process does not involve discretization of the predesigned path; instead, it iteratively searches for an optimal spatial point that ensures that the path strictly maintains the same spatial distance and linear constraints with respect to previous points. This search process also relies on the optimization objective function constructed in Section "Optimization-based conformal path planning."

The zigzag pattern, which is commonly used in 3D printing, is characterized by its broad applicability, high continuity, and ability to meet dense filling requirements that are

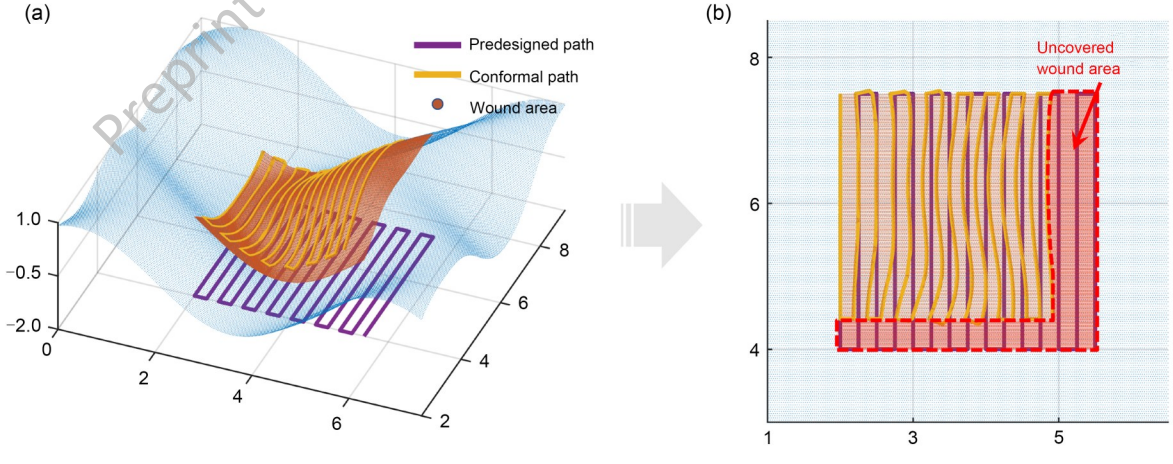

Fig. 2 Limitations of the conformal projection method for wound coverage. (a) Comparison of the predesigned and conformal paths projected onto the wound. (b) Top view showing a partially uncovered wound area

important for tissue repair [39]. Moreover, zigzag patterns have often been used for path pattern research related to bioprinting [40]. Therefore, in this study, we also use the zigzag pattern to develop a direct generation protocol for conformal repair paths. Fig. 3 shows a diagram of zigzag conformal paths plotted directly on a wound surface based on optimization principles. First, an initial point $P_{\text{init.}}$ and an initial direction $V_{\text{init.}}$ are determined according to the size and orientation of the wound area. Starting from $P_{\text{init.}}$, the next point is calculated stepwise on the surface with a spacing defined by point_space (also denoted as stp), until it exits the region of the wound. The generated initial dot array is then scanned along the orthogonal direction $V_{\text{orth.}}$ with line_space as the parameter until these waypoints traverse the entire area of the wound. The parameter line_space describes the spacing between two adjacent paths, and its value is dependent on the printing process.

The connection of adjacent paths also follows a stepwise optimization strategy, and uses $V_{\text{orth.}}$ and point_space as stepping parameters while ensuring right-angle turns. We also note that a secondary check between the waypoints and the boundary of the wound is necessary to ensure alignment (Fig. 3b3). If any points fall outside the wound area, their intersection with the boundary will be computed, or the nearest boundary point will be approximated to determine the waypoints. Additionally, considering the printed filament's width, inward indentation along the wound's edge is necessary, with the indentation parameter typically set to half the filament's width. Finally, the discrete waypoints are connected sequentially to generate a conformal printing path directly from the 3D point cloud of the surface.

2.2.2 Multi-layer path for wound filling

Layer-by-layer deposition is a fundamental process in 3D printing, and relies solely on acquired point clouds that provide path information for only a single layer. However, this poses significant limitations regarding addressing the volumetric filling and repair requirements of many injuries. A point cloud hole-filling algorithm based on radial basis functions (RBFs) is a well-established method that can be used to mend incomplete 3D models [41]. Briefly, it leverages boundary information from the holes in point clouds, and computes the average distances, angles, and curvature of the neighboring points. By searching for points that conform to prescribed patterns of variation among these three criteria, the algorithm progressively fills the hole until complete restoration is achieved. As used here, an RBF is an implicit surface that can be controlled by discrete points in a point cloud, thereby enabling smooth interpolation of scattered spatial data. In the context of injury repair tasks, the point cloud at the defect site is removed and an implicit surface is constructed using Gaussian-shaped basis functions. This in turn generates a point cloud that exhibits variations

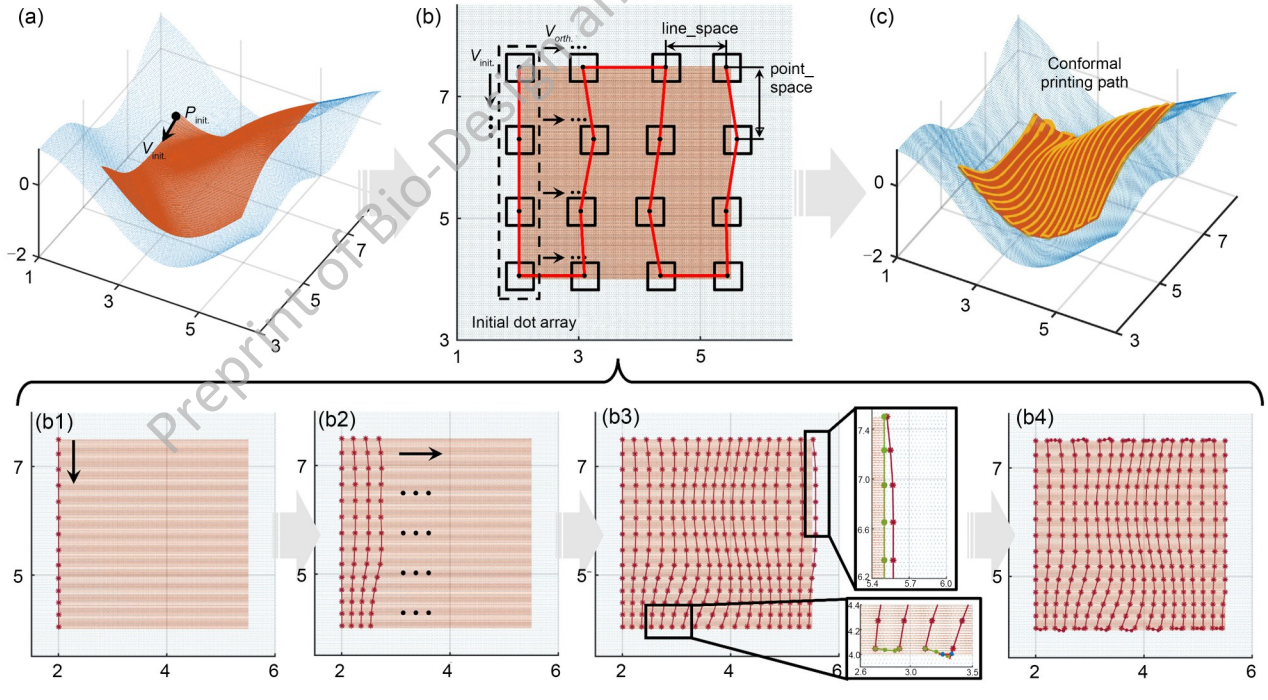

Fig. 3 Flowchart of direct conformal path generation produced by our optimization method. (a) Surfaces and wound regions (highlighted in red). (b) Generation of waypoints: (b1) generation of the initial dot array based on $V_{\text{init.}}$ and point_space; (b2) subsequent dot array generation based on $V_{\text{orth.}}$ and line_space; (b3) evaluation of edge dots based on the actual coverage area of the wound; (b4) sequential connection of all waypoints. (c) Conformal printing path in a zigzag pattern that covers the whole wound area

in curvature that are designed to be similar to healthy (i.e., uninjured) skin. The original point cloud is then subjected to Boolean operations on the interpolated points, resulting in an enveloping space that denotes the region that requires bioprinting-based filling.

The initial layer of the conformal path is generated on an original point cloud for the tissue injury using the method described in Section "Conformal path generation strategy for wound repair." According to the thickness of the printed filament, the second layer path can then be generated on the point cloud by offsetting the initial layer path along the normal direction at each waypoint. Points exceeding the surface of uninjured skin in the point cloud are filtered out, and what is left is the obtained point set for path planning. This approach ensures similarity of shape between a newly generated point cloud and the original wound, thus achieving conformal layering. The conformal path for the current layer is then planned using the same method. Next, to obtain point clouds for higher layers, normal vectors captured from the scanning data in the initial layer cannot be reused. Hence, a Kd-tree is used to organize the point cloud structure, and an approximate local normal vector for each point is calculated based on it. Moreover, the specific construction of the Kd-tree relies on the open-source library VLFeat [42]. We also note that for cases where the normal vectors of the wound are approximately parallel to the surface of healthy skin, newly generated point clouds produced using normal vector offsets may be smaller than the coverage area of the healthy skin, which can result in incomplete filling of the defect. In such situations, the overall principal component direction of the wound area can be used to offset the point cloud along the principal component direction; this can help to fill the incomplete area. Following this procedure, conformal layering and path planning steps are repeated until the volumetric injury is completely filled, as depicted in Fig. 4. Finally, the conformal paths produced using each layer are connected in sequential order according to the nearest neighbor principle, thereby achieving multi-layer conformal path planning for volumetric injuries.

2.3 Design and processing of point cloud models

This study involves four types of 3D models, i.e., ellipsoidal surface, mathematical surface, folded protrusion surface, and murine back wound models. The first three models were designed using computer aided design softwares (SolidWorks and Dassault Systems), exported as STL files, and subsequently converted into point cloud models using Geomagic Studio software (Geomagic, Morrisville, NC, USA). Point cloud redistribution was then performed to ensure uniform point cloud density across the models. In addition, each of these models was physically constructed using photosensitive 3D printing for practical validation of in situ printing. Moreover, the murine dorsal wound model was established by a previous study from our group [11], in which we created four wounds of different sizes, locations, and depths on the murine back. Next, a structured light 3D scanner (HSCAN-S, Thunk3D, China) was used to capture the wound model of complex skin tissue defects and to obtain 3D point clouds. Due to the small size of nude mice, it was not feasible to plan multi-layered paths on scanned point clouds, which presented a limitation regarding the effectiveness of the validation step of the proposed algorithm. Accordingly, the scanned point cloud model was scaled up by a factor of five to serve as an object for planning conformal paths for wound repair. Similarly, the upscaled model was then encapsulated and 3D-printed to create a physical model for practical validation (by printing) of the proposed path generation method.

2.4 Materials and hydrogel preparation

Methacrylate gelatin (GelMA) and lithium phenyl-2,4,6-trimethylbenzoylphosphinate (LAP) were purchased from EFL Inc. (Suzhou, China), and prepared as precursor solutions

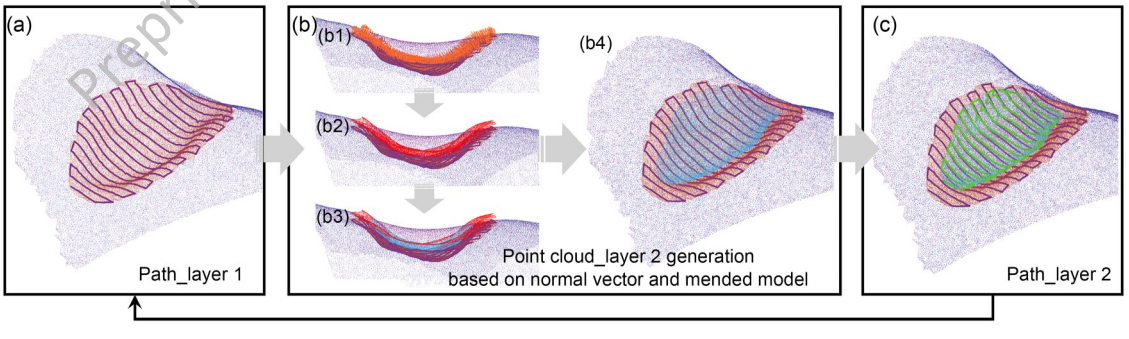

Fig. 4 Flowchart depicting multi-layer conformal path generation. (a) Generation of path_layer 1 using the original point cloud. (b) Strategy for generating point cloud_layer 2: (b1) obtaining the normal vector of the path based on path_layer 1 and the original point cloud; (b2) generating point cloud_layer 2 based on normal vectors and the layer thickness; (b3) obtaining the intersection of point cloud_layer 2 and the RBF-repaired point cloud; (b4) obtaining the final point cloud_layer 2 that defines the region to be repaired. (c) Generation of path_layer 2 on point cloud_layer 2. RBF: radial basis function

according to the manufacturer's instructions. Briefly, a predetermined amount of lyophilized GelMA was weighed and thoroughly dissolved under magnetic stirring in phosphate-buffered saline (PBS) containing 0.5% LAP at 40 °C, resulting in a final GelMA concentration of 10%. Edible dye was then added to enhance its visibility, and the prepared solution was stored at 4 °C for further use.

2.5 Experimental setup and printing process

The printing device used for this study is a seven-axis bioprinting robot whose development has been previously reported [14, 43]. Its serial structure and redundant configuration demonstrate advantages such as favorable manipulability for in situ bioprinting, and it possesses a trajectory tracking accuracy of approximately 0.17 mm [14]. However, differences between this device and alternatives include the simplification of its printing end effector. Specifically, applying Ruhr needles shortens the length of the actuator and reduces the distance that the bioink travels during injection. This adjustment is designed to reduce the influence of shear effect on hydrogel condition during the printing process [44], thereby allowing for a better illustration and comparison regarding the impact of path planning on printing outcomes. The printed hydrogel structure then undergoes temporary deposition via a thermosensitive process. Upon completion of printing, secondary curing is performed via irradiation with a light-emitting diode (LED) surface light source of 405 nm wavelength (light irradiance: 100 mW/cm^2; exposure time: 20 s). Next, a final end effector is installed at the flange of the seven-axis robot. By employing tool center point (TCP) calibration, the homogeneous transformation matrix of the end effector can be obtained and then incorporated into the proposed robot kinematic control algorithm [14]. The designed printing targets were manually created and aligned with the coordinate system of the bioprinting robot for subsequent printing experiments.

During the printing process, ensuring uniform filament deposition requires maintaining a consistent TCP velocity across the surface. However, the mapping between the TCP and joint velocities can be highly nonlinear [45]. The methodology for planning the robot's printing trajectory was guided by the results of a previous study [46]. In simple terms, the generated path was divided into uniformly spaced discrete points, which allowed the TCP to move at a consistent speed between adjacent points. Furthermore, to ensure continuous changes in TCP orientation, we introduced a tolerance (θ_t) for the printing angle. The introduced tolerance θ_t ensures that the printing nozzle remains within a conical region defined around the surface normal vector. By selecting appropriate nozzle orientations within this region, the priority is given to ensuring uniform and continuous linear speed along the entire path.

2.6 Printing experiment analysis for the path planning algorithm

Next, we evaluated the path planning algorithm using actual printing and image analysis experiments. First, the line_space parameter was determined based on the printing filament width, thereby ensuring that material printed along a specified path can precisely cover the area of the reference trajectory. This is critical, since traditional projection-based path planning approaches may lead to overfilling or underfilling defects in curved surface printing. Therefore, printing paths are separately designed using both the traditional method and the optimization-based approach proposed in this study, followed by 3D printing experiments for validation. After printing, top-view photographs of the printed structures were captured with a camera and subsequently analyzed using ImageJ.

Quantitative evaluation of the printing effectiveness relied primarily on three parameters: S_d, which refers to the area covered by the designed trajectory and was used to represent the intended printing area; S_e, the area covered by extending the planned path along the line width; and S_p, the coverage area of the printed structure. The fidelity of in situ bioprinting on this curved surface can be evaluated by examining the relationship between S_e and S_p, which indicates whether the printed structure matches with the theoretically designed one. Similarly, the effectiveness of the planned path in achieving complete coverage of the surface can be evaluated by examining the relationship between S_d and S_p, which assesses whether the printed structure exhibits overfilling or underfilling deficiencies and whether it can achieve high-precision coverage of the wound area.

2.7 Printing experiment analysis of the wound repair path

To analyze the results of the printing experiments, in which the wound repair path was plotted on a dorsal wound model, the first step involved removing the wound area from the obtained point cloud model. Next, using an RBF hole-filling algorithm based on the curvature of healthy skin areas, the missing skin can be filled to generate a simulated healthy dorsal skin model. Subsequently, using the method described in Section "Multi-layer path for wound filling," multi-layered printing paths were generated for different wounds to guide the seven-axis bioprinting robot for in situ bioprinting. After physical printing, the 3D scanner was employed again to capture the surface point cloud of the printed model. We then imported this model and the RBF-filled model into Geomagic Studio software, and registered both based on their respective feature points. Upon completion of the registration process, the built-in deviation calculation function was used to compute deviation heatmaps between the two models, thereby

providing an assessment of the accuracy of the bioprinting process for wound repair.

3 Results and discussion

3.1 Selection and analysis of step size parameters

As described in Section "Optimization-based conformal path planning," during the optimization of the printing path, the search step size stp is one parameter that can influence alignment consistency between the path and surface. As shown in Fig. 5a, when a predefined flat path is mapped onto the surface, taking three intermediate points as examples, the distance between these points on the flat path is stp, and they produce an angle of 180°. However, when mapped onto the surface, the objective of the constraint is to ensure that the distance between adjacent points along the surface is stp. Moreover, the Euclidean distance between them, which is calculated by $\| SP_i - SP_{i-1} \|$ (i.e., stp_r), is inevitably not equal to stp, leading to quantifiable distance errors (Fig. 5b). At the same time, all three mapped points are present on the curved surface. The convexity of this surface makes it challenging to faithfully project angles, meaning that it may not be possible to ensure that the angles add up to 180°. This issue is ineluctable and can be mitigated only by selecting an appropriate stp to minimize both distance and angle errors. For example, in Fig. 5c, as the step size stp decreases from 3 to 1, the overall deviation J also decreases, with the reduction primarily contributed by the angular deviation J_a.

Overall, decreases in stp lead to increases in computation complexity and consequently increased computation time. To further explore trends in error and computational complexity caused by varying values of stp, we conducted path mapping and statistical analyses on ellipsoidal, mathematical, and origami surfaces using different stp values, as shown in Figs. 5d–5f. These results consistently showed that as stp decreases, the required computational complexity exponentially rises. Moreover, reductions in error are eventually limited as stp is further reduced, making further reductions a nonviable tradeoff. Next, error and computation time were plotted together, and the intersection point of these two curves was initially chosen as the optimal stp value, since it simultaneously achieved lower mapping error and computational complexity. Furthermore, the optimal stp values for each of the three surfaces and their respective point cloud densities are listed in Table 1, and analyses of these data resulted in the construction of the following empirical equation.

$$Density * l_{opt} * w_{opt} \approx 20 \tag{5}$$

Here, l_{opt} equals to optimal stp, and w_{opt} equals to half of the optimal stp, as described in Section "Conformal mapping with shape preservation."

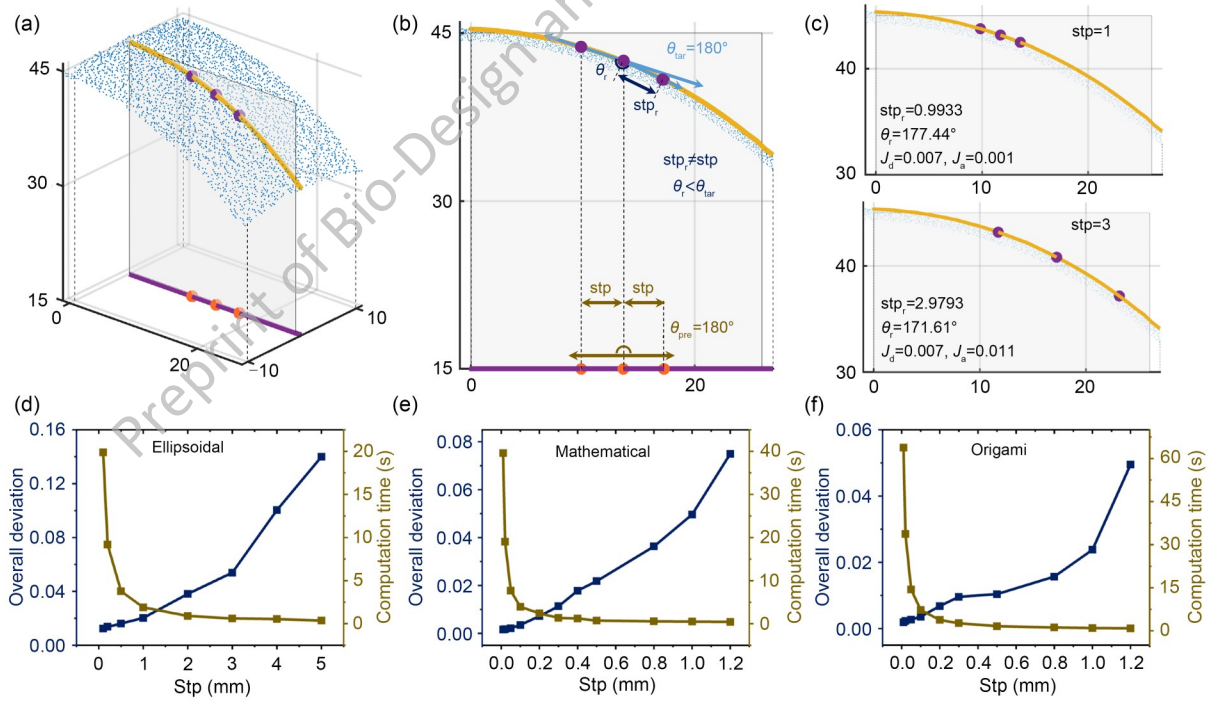

Fig. 5 Effect of step size on projection. (a) Overall schematic. (b) Projecting planar waypoints onto a surface changes both stp_r and θ_{tar} due to surface curvature. (c) Values for stp_r, θ_{tar}, and overall deviation J (J_a+J_d), obtained from different stp values. (d–f) Trends of overall deviation J and computation time at different stp values for ellipsoidal (d), mathematical (e), and (f) origami surfaces. stp: the preset searching step distance; stp_r: the real Euclidean distance between adjacent points; θ_{tar}: the target angle; θ_r: the real angle

Table 1 Summary of point cloud density and optimal stp

Surface type	Density (cm^{-2})	Optimal stp (mm)	J	Computation time (s)
Ellipsoidal	1.5×10^4	1.30	0.0249	2.36
Mathematical	1.1×10^5	0.210	0.00942	2.45
Origami	1.8×10^5	0.110	0.00364	6.25

J: overall deviation; stp: the preset searching step;

Equation (5) indicates that for any surface of a given density, the stp value obtained using the method described here strikes a balance between computation speed and error reduction, suggesting that this is favorable for generating optimal step size values for path generation. This provides valuable guidance for selecting step lengths during optimization-based conformal path generation on unknown surfaces. The theoretical basis of Eq. (5) is as follows. First, it represents the ideal number of scattered points within the ROI. As described in Section "Conformal mapping with shape preservation," both the length and width of the ROI are denoted by stp. With respect to dimensions, the multiplication of the length and width cancels out the denominator associated with the density dimension, thereby leaving the number of scattered points as the unit. Moreover, there are approximately 20 points in each ROI, and this is sufficient to fit to a quadratic surface. This point is supported by other studies [47–49], and theoretically reinforces the applicability of the proposed empirical formula.

3.2 Comparison between the conformal and direct-projected paths

We note that the pursuit of conformality in projecting planar paths onto curved surfaces holds practical significance. For instance, for path planning based on zigzag patterning during 3D printing, a consistent spacing of the curves aids in achieving uniform filament deposition, thereby preventing printing defects such as overlaps or gaps. As shown in Fig. 6a, when the zigzag path is mapped onto an ellipsoidal surface using different approaches, the curvature increase underneath the ellipsoid can cause the spacing d_d of the paths generated using the direct projection method to widen, thereby leading to a loss of its equidistant characteristic. Moreover, integrating the constraint of the preserving angle into account, right-angle turns in the zigzag path can be spatially optimized according to the surface characteristics, as illustrated in Fig. 6b. The necessity of preserving angles is even more apparent in manufacturing applications of conformal antennas. These include the construction of conformal antennas on surfaces using the 3D direct-write approach, where even subtle changes in morphology can lead to alterations in the electrical properties of the antennas [50, 51].

As shown in Fig. 6c, when directly projected onto an ellipsoidal surface, square spiral curves with multiple right-angle turns experience distortion in certain corners, with the most notable resulting in a change from 90° to 50.3°. However, spatial paths generated under conformal constraints can maintain

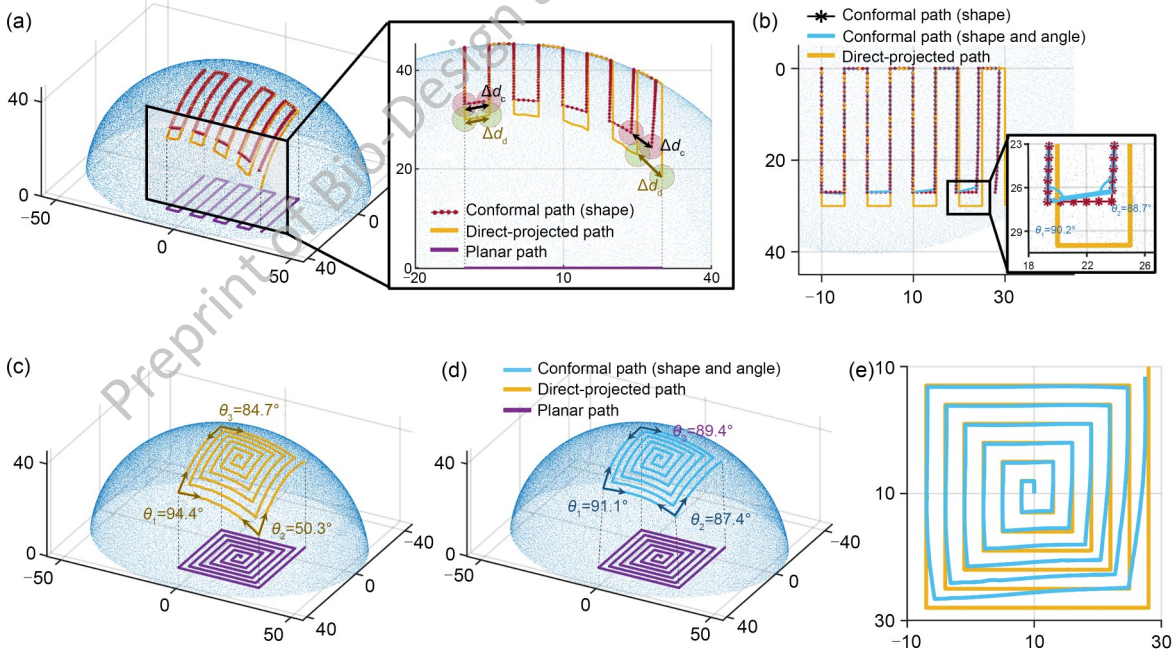

Fig. 6 Comparison between conformal and direct-projected paths. (a) Conformal path with shape preservation for maintaining equidistant curves. Δd_c: the distance between zigzag patterns in conformal path; Δd_d: the distance between zigzag patterns in direct-projected path; (b) Conformal path with shape and angle preservation. (c) Distortions created for a direct-projected path with right angles. (d) Conformal path preserving right angles. (e) Top-view comparison of conformal and direct-projected paths

turn angles near 90°, with a maximum deviation maintained under 0.05 rads (Fig. 6d). Next, a top-view comparison of these two paths is illustrated in Fig. 6e. The practical value of this angle preservation has also been confirmed by studies conducted by Adams et al., who demonstrated its significance for printing-based fabrication of spherical antennas [51].

3.3 Conformal mapping from plane to surface

To explore the applicability of the proposed conformal path planning method for different types of curves and surfaces, further testing was conducted based on the presets outlined in Section "Examples of conformal path generation on 3D surfaces." Specifically, three pre-planned complex planar paths were conformally mapped onto three types of point cloud surfaces. During the stepwise searching process for conformal points, Eq. (5) was employed to select suitable stp values for each surface. When using the optimization-based conformal path generation strategy, all spatial paths demonstrated high conformality, as indicated by the green lines in Fig. 7. The corresponding relative errors, all of which fell within the order of 10^{-2}, are listed below their respective images. Moreover, the maximum angular deviation for all demonstrations did not exceed 0.1 rads, and the time required for generating all conformal paths was within 6 s. Correspondingly, the surface paths generated using the direct projection approach are presented in Fig. 7 by red lines. A comparison between the top views of the zigzag and square spiral paths reveals that our proposed conformal strategy resulted in a more faithful reproduction of curve equidistance and right-angle elements. Furthermore, when applying the direct projection approach, distortions in pattern may occur, and these can potentially lead to defects during the printing process. This issue will be further explored in subsequent practical printing experiments.

3.4 Bioprinting validation and analysis on geometric models

Thus far we have confirmed the comprehensive advantages of the proposed conformal path planning method with respect to the optimization procedure for step size parameters as reported in Section "Selection and analysis of step size parameters," the superiority of the conformal path over the direct-projected path as reported in Section "Comparison between the conformal and direct-projected paths," and the validation of this approach's applicability across various curves and surfaces as reported in Section "Conformal mapping from plane to surface." Next, it is necessary to evaluate the effectiveness of the planned paths in guiding in situ bioprinting and to confirm the advantages of conformal paths in reducing printing defects based on the practical printing results.

To do so, three representative patterns in Section "Conformal mapping from plane to surface" were selected for

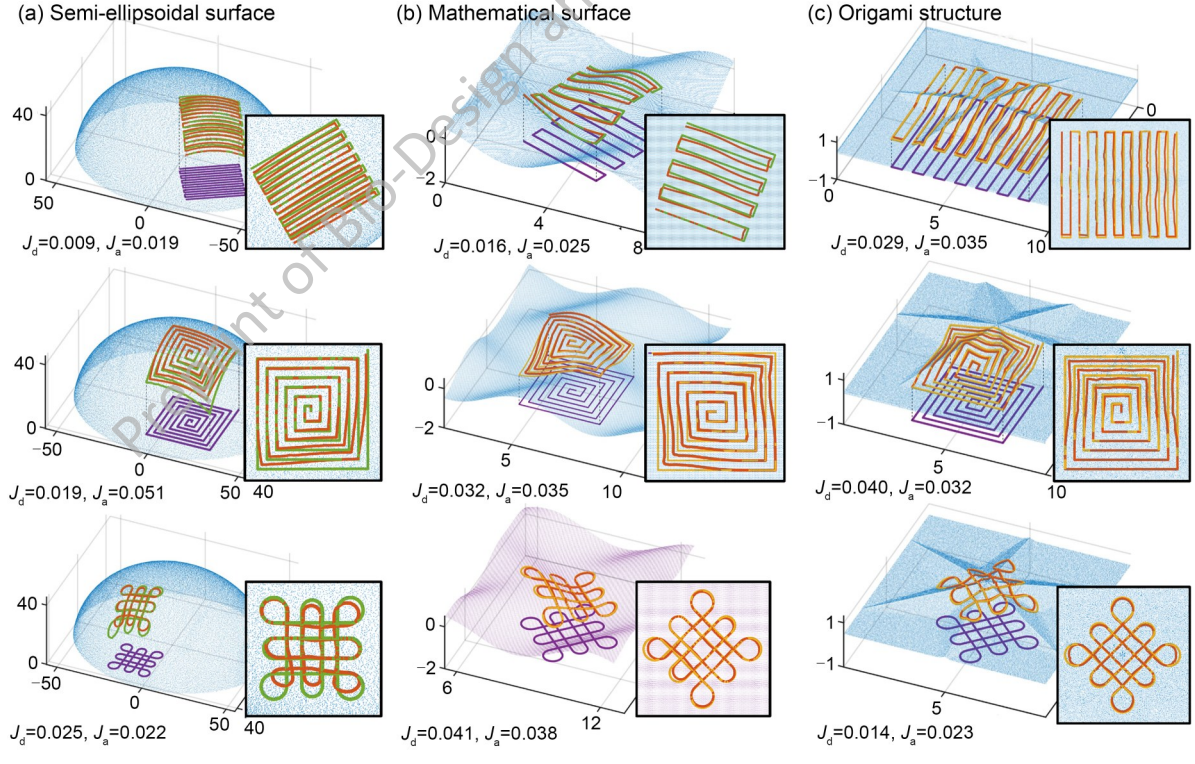

Fig. 7 Conformal mapping illustrations from plane to surface. (a) Semi-ellipsoidal surface. (b) Mathematical surface. (c) Origami structure. Deviations are listed below each image, with J_d representing the distance deviation and J_a representing the angle deviation

practical bioprinting experiments to validate the effectiveness of the conformal paths in guiding in situ bioprinting. Figs. 8a1–8c1 show the predesigned conformal paths on point cloud surfaces, while Figs. 8a2–8c2 depict the actual printing results. Preliminary assessment of these photos suggests that the proposed in situ bioprinting strategy, which encompasses the use of specific materials and equipment, as well as specific path generation method, can construct the desired patterns on complex surfaces with high fidelity, closely aligning with predetermined paths. The quantitative evaluation, as described in Section "Printing experiment analysis for the path planning algorithm," involves extending the top view of predetermined paths by the width of the printing filament, i.e., 0.18 mm. The resulting area S_e and the actual printed area S_p are depicted in green and blue, respectively. In the three examples presented here, the pixel areas occupied by S_e and S_p are essentially the same. Moreover, independent testing of three distinct cases revealed average deviations S_p/S_e of approximately 96.9%±1.6%, 97.2%±0.8%, and 95.5%±2.1% (Figs. 8a3–8c3). Furthermore, despite the existence of specific variations that depended on the curvature of the surface and the characteristics of the predefined path, overall this process consistently demonstrated high fidelity.

Subsequently, a comparison was performed between conformal paths and paths generated using a traditional direct projection method using a dense filling approach (Fig. 9). In both cases, zigzag patterns were employed for path planning on various surfaces, and the line spacing was determined by the filament diameter, i.e., 0.18 mm. In each case, the left side depicts the results of the conformal path, while the right side illustrates that of direct-projected path. The practical coverage areas were still calculated and are juxtaposed with the designated coverage area outlined by dashed lines. These results indicate that for the printing process with the direct-projected path, defects involving insufficient filling commonly occur in regions with significant curvature changes, such as the troughs of mathematical surfaces or the corners of folded structures. Moreover, the ratios between S_p and S_e indicate that in densely arranged conformal paths, the printing replicability remains around 98.1%±0.7%, once again demonstrating the stability of the in situ bioprinting process. In contrast, the direct-projected paths exhibited a lower coverage rate of the preset area of approximately 93.6%±2.1%, mainly due to the presence of gap defects. The area of these gaps, denoted here as S_h, was also calculated, and is annotated in the corresponding figures. Overall, it

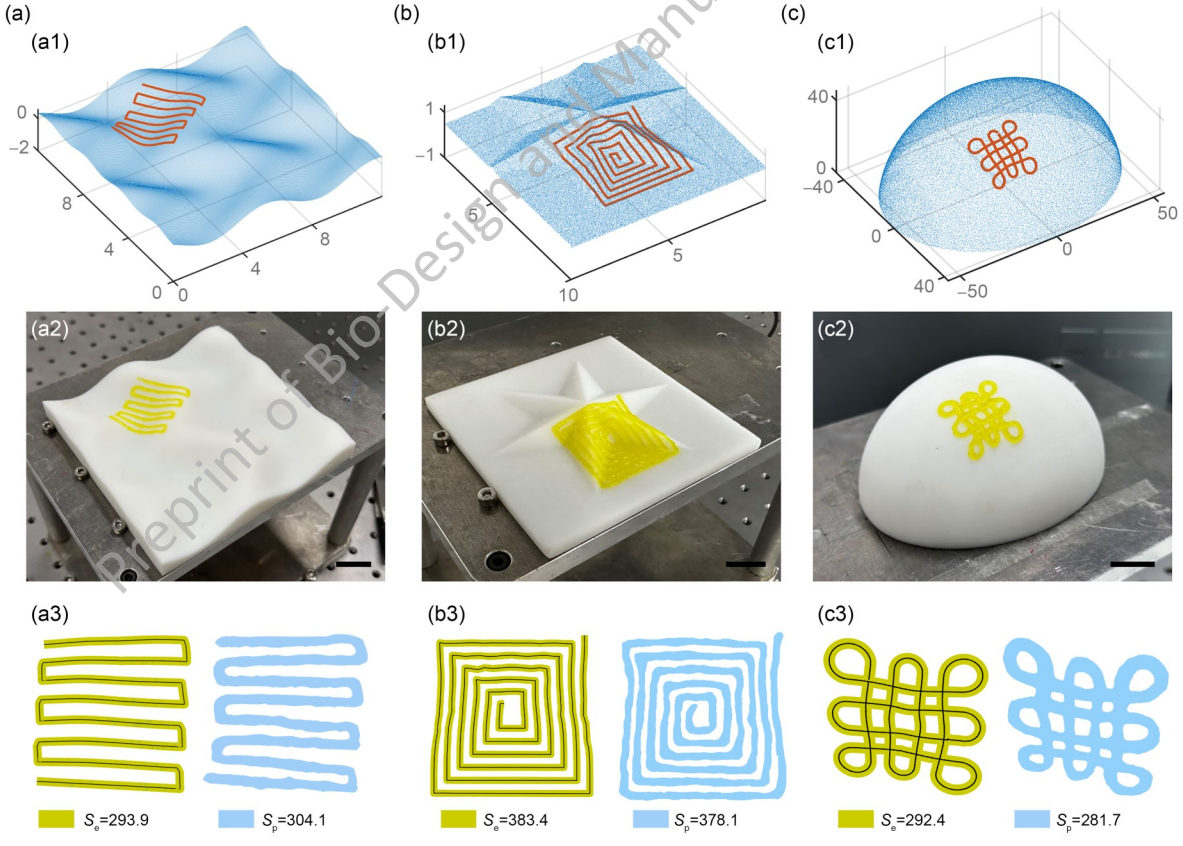

Fig. 8 Bioprinting validation using geometric models. (a) Zigzag path on a mathematical surface: (a1) model generated using MATLAB; (a2) actual printed image; (a3) comparison of the theoretical coverage area and the actual coverage area. (b) Square spiral path on an origami structure. (c) Chinese knot pattern on an ellipsoidal surface. Figs. b1–b3 and c1–c3 represent the same image types as Figs. a1–a3 (scale bars for subplots a2–c2: 2 cm). S_e: the area covered by extending the planned path along the line width; S_p: the coverage area of a practical printed structure

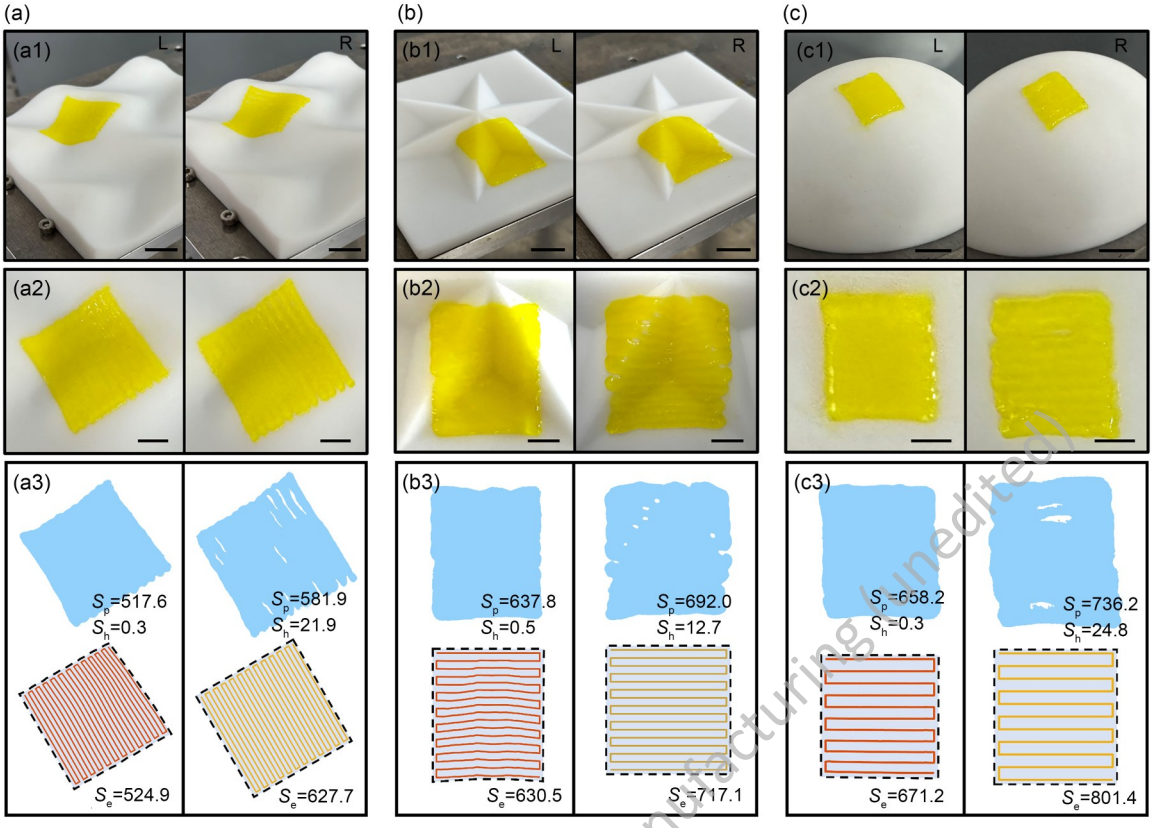

Fig. 9 Dense pattern bioprinting path validation on geometric models. (a) Zigzag paths on mathematical surfaces: (a1) actual printed image; (a2) top view of the actual printed image; (a3) comparison of the actual coverage area and the theoretical coverage area. (b) Zigzag paths on an origami structure. (c) Zigzag paths on an ellipsoidal surface. Figs. b1–b3 and c1–c3 represent the same image types as Figs. a1–a3 (scale bars for subplots a1–c1: 2 cm; and for subplots a2–c2: 1cm). L: left, representing the conformal path method; R: right, representing the direct projection method; S_e: the area covered by extending the planned path along the line width; S_p: the coverage area of the practical printed structure; S_h: the area of underfilled gaps in the printed structure

occupies about 3.1%±1.2% of the preset area, although the precise proportion varies with surface type and local curvature. Taken together, these practical printing experiments collectively affirm the necessity of constructing conformal paths for in situ bioprinting conducted on curved surfaces.

3.5 Bioprinting validation and skin wound model analysis

The above section demonstrates the effectiveness of the proposed method for guiding high fidelity in situ printing on 3D surfaces. Next, we focused on practical application scenarios related to skin wound repair. This involved directly generating multi-layer conformal paths within complex skin wounds to guide the repair process via in situ bioprinting. To generate conformal paths on irregular and complex point clouds, as illustrated in Fig. 10, we used an approach similar to that described in Fig. 3. Moreover, it is essential to note that path planning generally followed the principal component direction of the wound, thereby aiding in achieving better wound coverage using a dense pattern [19, 52]. Moreover, once the principal direction is determined (Fig. 10c1), a point-by-point search was conducted along the orthogonal direction for the widest part of the wound to construct an initial dot array. The search then extended along the principal direction on both sides until the point cloud is comprehensively covered; moreover, this process was constrained by the requirement of maintaining equidistant curves (Fig. 10c2). Finally, waypoints located inside the point cloud were preserved and connected sequentially to form a zigzag conformal path that covers irregularly-shaped wounds (Fig. 10c3).

As described in Section "Conformal path generation strategy for wound repair," during the generation of repair paths that use zigzag patterns to cover the wounds, the adjustable parameters describing the zigzag path include point_space, line_space, and indentation. However, due to point-to-point motion patterns of the bioprinting robot, an excessively large point_space can result in mismatches between the zigzag path and the complex surface. Moreover, conformal paths with different parameters on the point cloud defining the skin wound also demonstrate how poor point_space values can generate mismatches (Figs. 11a – 11c). In this context, the point_space and step size (stp, optimized in Section "Selection

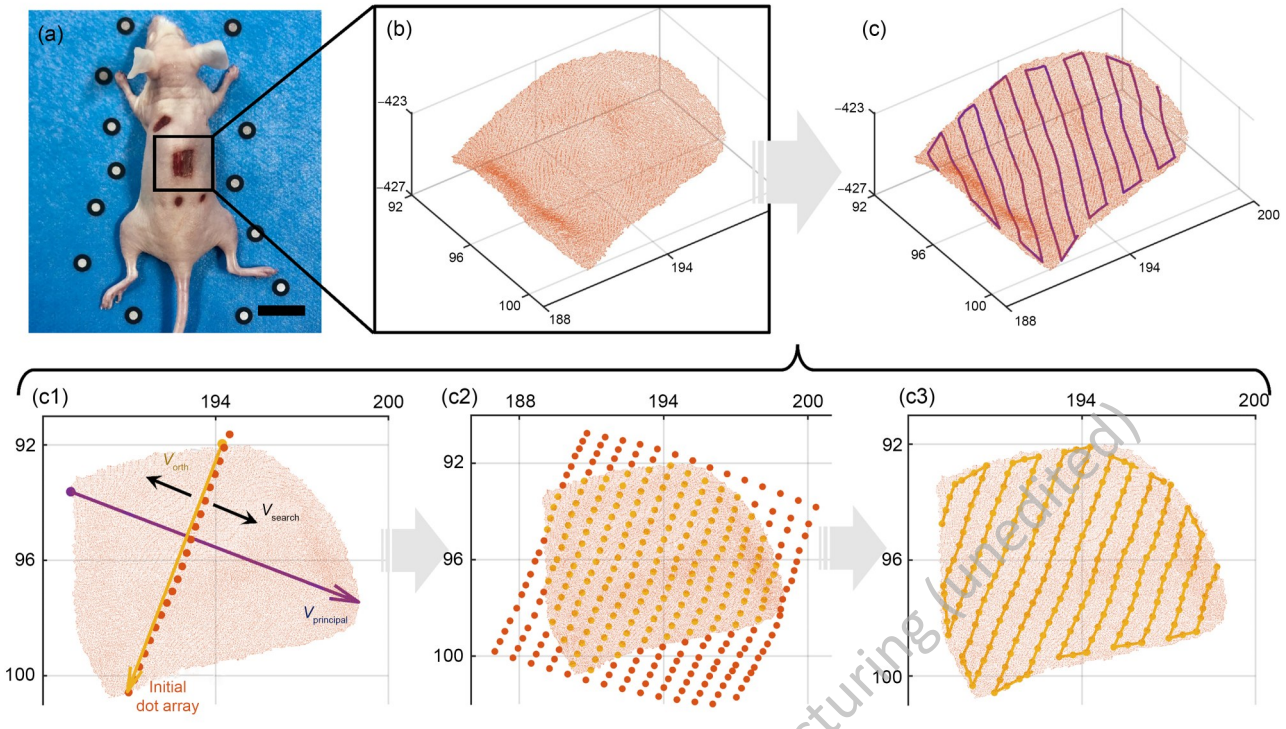

Fig. 10 Conformal path generation strategy for actual wound coverage. (a) Image of a mouse with induced back wounds (scale bar: 2 cm). (b) Three-dimensional scanned point cloud for one of the wounds. (c) Conformal path generation for complete wound coverage: (c1) determination of the search direction and initial dot array based on the principal component direction and the widest region of the wound; (c2) extension of the initial dot array along the search direction until complete coverage of the entire wound is achieved; (c3) exclusion of waypoints outside the wound, followed by sequential connection of all points. V_{search}: the searching direction; V_{orth}: the orthogonal direction of the searching direction; $V_{principal}$: the searching direction along the principal components of the point cloud

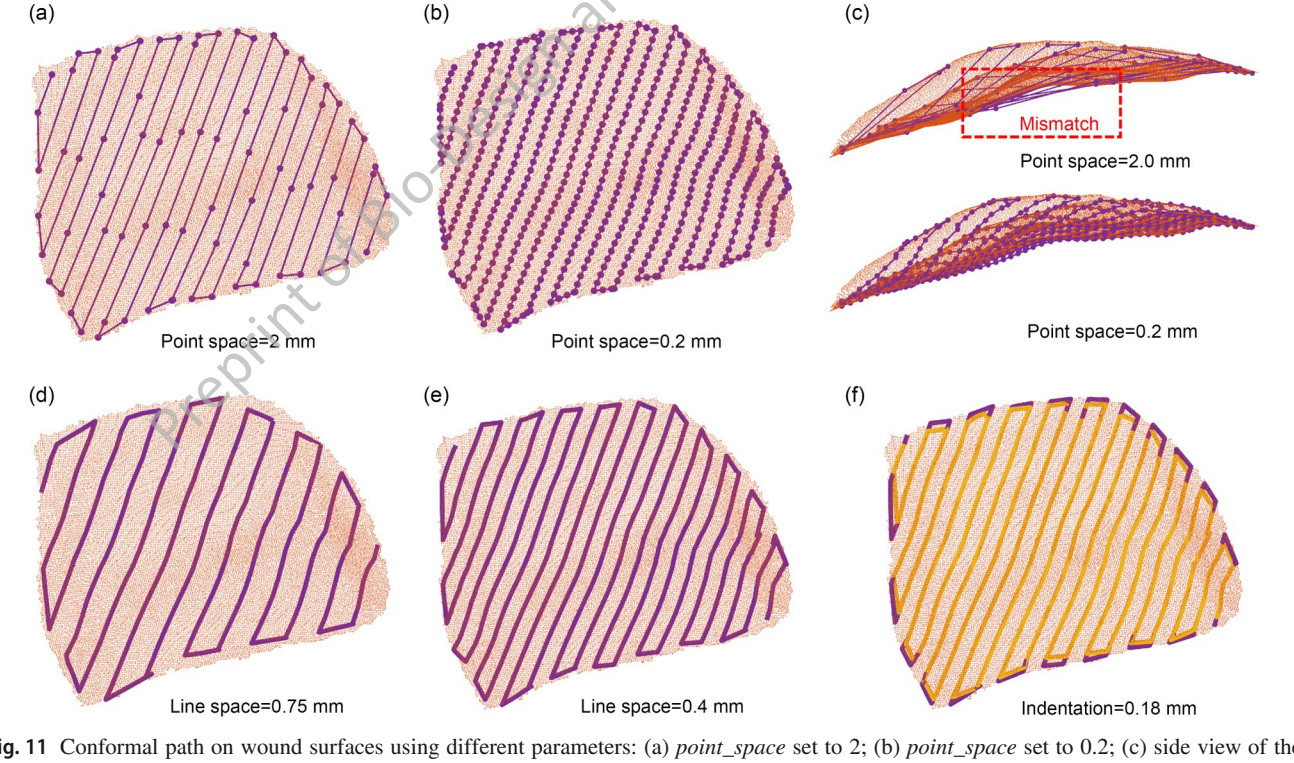

Fig. 11 Conformal path on wound surfaces using different parameters: (a) *point_space* set to 2; (b) *point_space* set to 0.2; (c) side view of the path and surface, showing mismatches in regions of high curvature; (d) *line_space* set to 0.75; (e) *line_space* set to 0.4; (f) indentation parameter set to 0.18

and analysis of step size parameters") parameters have consistent effects, aiming to achieve high levels of similarity between the generated path and the target surface to be repaired. Therefore, for a known density of determined point clouds, setting point_space equal to stp can result in optimal high fidelity in situ bioprinting outcomes. Furthermore, the line_space parameter determines the search distance on both sides of the initial dot array. Since generating a dense arrangement of printed threads can be necessary when filling and treating skin wounds [27, 52], it is essential to define the line_space parameter using preliminary experiments before path planning. Figs. 11d–11e showcase repair paths using different line_space values. However, when determining line_space and then expanding the initial dot array on the surface based on its value, it is advisable to avoid using line_space as the search step. Normally, the line_space parameter is typically larger than point_space (stp), and therefore leads to an increase in mapping error due to the larger search step. Accordingly, during the expansion process of the initial dot array, line_space is divided into multiple segments based on stp. The search for target points at a fixed value of line_space relative to the starting point was still conducted using stp as the step size, thereby ensuring equidistant characteristics during the expansion. We also note that indentation is also a vital parameter. To ensure precise alignment between the printed structure and the boundaries of the wound, the original planned path must be shrunk by a certain width. Using 0.18 mm as an example, the comparison between the shrunken and original paths is illustrated in Fig. 11f.

For the skin wounds generated for analysis, achieving complete wound coverage often necessitated multi-layer path planning. Using the model processing method described in Section "Printing experiment analysis of the wound repair path" and the multi-layer path generation strategy outlined in Section "Multi-layer path for wound filling," the area to be repaired is delineated by blue and deep red borders (Figs. 12b–12d). The thickness of the printing filament (normally 1 mm) and the actual depth of the wound dictate the

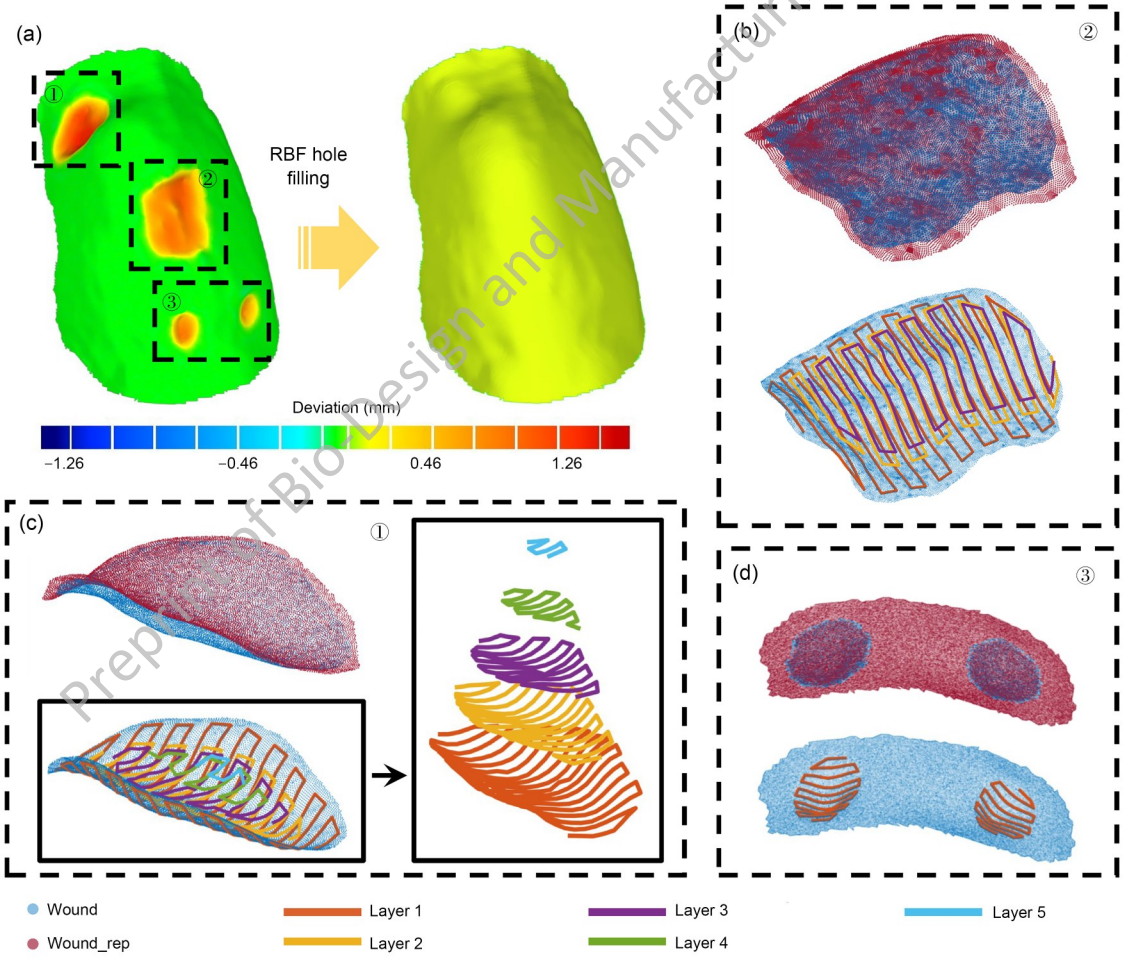

Fig. 12 Multi-layer path planning for mouse back wound models. (a) The RBF method was used to fill the scanned mouse back wound into a smooth model surface, thereby simulating an undamaged skin state. (b) The areas to be filled and the planned multi-layer paths for Wound 2. (c) The areas to be filled and the planned multi-layer paths for Wound 1. (d) The areas to be filled and the planned conformal paths for Wound 3. RBF: radial basis function; Wound_rep: wound to be repaired

number of printing layers, and these continue until the wound is completely filled. The final obtained wound repair paths are depicted in Fig. 12. For instance, Wound 1 involved five path layers, while the smaller Wound 3 required only one layer for treatment. In addition, for the conformal paths, the normal vector of each waypoint aligns with the surface normal vector, thereby constraining the posture of the end effector of the bioprinting robot. This ensures that during the bioprinting process, the robot's nozzle adapts to changes in the local surface normal vector as it moves along the path. For in situ bioprinting, a strategy of increasing the printing angle (i.e., the angle between the printing nozzle and the surface tangent) can achieve more precise bioink deposition [53].

The actual printing process is depicted in Fig. 13. The upper left image depicts an overview of the printing setup, where the end effector of the seven-axis bioprinting robot is an advanced tool capable of quantitatively extruding a bioink. Fig. 13b presents the process for repairing Wounds 2 and 3, while the comparison between Figs. 13b1 and 13b2 highlights the deposition of multiple layers of the hydrogel. Similarly, Fig. 13c illustrates the complete process for repairing Wound 1, with images corresponding to specific layers as follows: 1 layer (Fig. 13c1), 2 layers (Fig. 13c2), 3 layers (Fig. 13c3), 4 layers (Fig. 13c4), and 5 layers (Fig. 13c5). The outcome of this process is the complete filling of the wound. Next, by observing these printing results for Wound 1 in an inclined orientation, despite the strict alignment of the nozzle with the wound surface during the printing process, positional shifts may occur after bioink is extruded due to insufficient temperature-sensitive crosslinking and

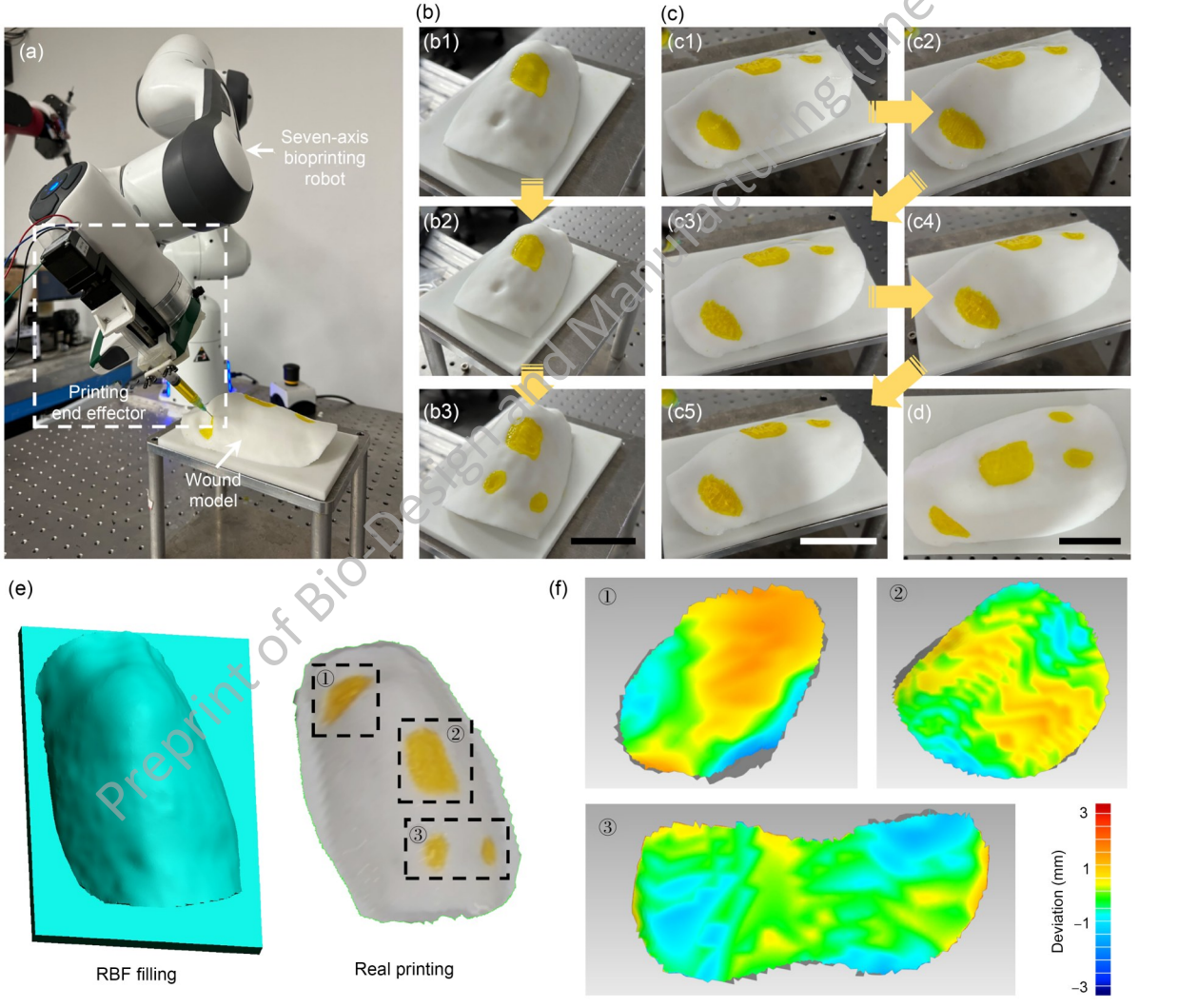

Fig. 13 In situ bioprinting on a mouse back wound model. (a) Photograph of the seven-axis bioprinting robot and the model used in this experiment. (b) Process images during printing and repair of Wounds 2 and 3 (scale bar: 5 cm). (c) Process images during printing and repair of Wound 1 (i.e., the deepest wound studied, scale bar: 5 cm). (d) A bioprinting-repaired back wound model (scale bar: 5 cm). (e) Comparison between the back model after RBF repair and the 3D scanned model after bioprinting repair. f, Comparative images showing differences among various wounds. The average deviations for Wounds 1–3 are (0.90±0.74) mm, (0.52±0.49) mm, and (0.53±0.70) mm, respectively. The maximum deviation observed is 2.12 mm. 3D: three-dimensional

gravitational effects on the extruded filament. In the future, upgrading the printing end effector for simultaneous photocrosslinking after extrusion [54] may enhance the crosslinking stability of the hydrogel, thereby mitigating the tendency for structural downward sliding observed in the current version of in situ bioprinting process.

A quantitative evaluation of the printing results was then conducted following the description in Section "Printing experiment analysis of the wound repair path" (Fig. 13e). The dimensional discrepancies after repairing the three wounds are statistically presented on the right and show average deviations of (0.90±0.74) mm, (0.52±0.49) mm, and (0.53± 0.70) mm for Wounds 1–3, respectively, as well as a maximum deviation of 2.12 mm (Fig. 13f). Despite inherent errors of the 3D scanner and deviations introduced during the registration of the two models, the skin-like structure constructed using in situ bioprinting essentially reproduces the appearance of undamaged skin. Here we observed no significant boundaries between the wound edges and the printed structure, indicating the high degree of conformity between the constructed structure and the shape of the wound. Further quantitative analysis suggests the feasibility of guided conformal path planning algorithms for in situ bioprinting, further highlighting the potential of this study to improve 3D bioprinting methods for treating skin injuries.

4 Conclusions

In conclusion, this study introduces an effective conformal path planning algorithm based on optimization principles. This algorithm was then used to demonstrate effective and accurate path generation for in situ bioprinting on a complex and irregular surface. This algorithm, which meticulously balances both shape and angle preservation, generates paths that faithfully replicate original planar designs, thereby minimizing errors with respect to both distance and angle. Systematic analysis of the step size parameter sheds light on the crucial trade-off between computational complexity and mapping error. Furthermore, comparative evaluations against direct-projected paths highlight the advantages of this algorithm for maintaining equidistance and angle fidelity, features that may be particularly significant for applications such as 3D bioprinting and antenna fabrication. Moreover, the efficacy of this algorithm was validated during final practical bioprinting experiments, including applications on diverse surfaces and complex skin wounds. Furthermore, the in situ bioprinting process consistently presented high fidelity during the reproduction of predetermined paths, thereby ensuring minimal deviation and effective wound coverage.

Overall, this research contributes to the progression of in situ bioprinting technologies and provides a systematic approach for precise path planning on irregular surfaces. The proposed algorithm opens avenues for customizable treatments of volumetric injuries and emphasizes the potential posed by advancing 3D bioprinting to treat various tissue types and injuries. Future work may involve refining the printing process, exploring additional optimization strategies, and extending applications to broader medical contexts.

Acknowledgements This work was supported in part by the National Key Research and Development Program of China under Grant No. 2023YFB4302003, and in part by the National Natural Science Foundation of China under Grant No. 52205532.

Author contributions Conceptualization: WXZ and CXH; methodology: WXZ, CXH, and YNW; formal analysis and investigation: WXZ, YNW, and SZL; writing—original draft preparation: WXZ; writing—review and editing: all authors; funding acquisition: CXH, ZW; resources: CXH; supervision: CXH and TX.

Declarations

Conflict of interest The authors declare that they have no conflict of interest.

Ethical approval Ethical approvalThis study, including all the procedures involving animals that it entailed, were approved by the Animal Ethics Committee of the Tsinghua Shenzhen International Graduate School.

References

1. Venus M, Waterman J, McNab I (2010) Basic physiology of the skin. Surgery 28(10):469–472. https://doi.org/10.1016/j.mpsur.2010.07.011
2. Sun BK, Siprashvili Z, Khavari PA (2014) Advances in skin grafting and treatment of cutaneous wounds. Science 346(6212): 941–945. https://doi.org/10.1126/science.1253836
3. Shpichka A, Butnaru D, Bezrukov EA et al (2019) Skin tissue regeneration for burn injury. Stem Cell Res Ther 10(1):1–16. https://doi.org/10.1186/s13287-019-1203-3
4. Tarassoli SP, Jessop ZM, Al-Sabah A et al (2018) Skin tissue engineering using 3D bioprinting: an evolving research field. J Plast Reconstr Aes Surg 71(5):615–623. https://doi.org/10.1016/j.bjps.2017.12.006
5. Daikuara LY, Chen XF, Yue ZL et al (2022) 3D bioprinting constructs to facilitate skin regeneration. Adv Funct Mater 32(3): 2105080. https://doi.org/10.1002/adfm.202105080
6. Weng TT, Zhang W, Xia YL et al (2021) 3D bioprinting for skin tissue engineering: current status and perspectives. J Tissue Eng 12:20417314211028574. https://doi.org/10.1177/20417314211028574
7. He P, Zhao JN, Zhang JM et al (2018) Bioprinting of skin constructs for wound healing. Burns Trauma 6(1):5. https://doi.org/10.1186/s41038-017-0104-x
8. Zhao WX, Hu CX, Xu T (2023) In vivo bioprinting: broadening the therapeutic horizon for tissue injuries. Bioact Mater 25:201–222. https://doi.org/10.1016/j.bioactmat.2023.01.018
9. Singh S, Choudhury D, Yu F et al (2020) In situ bioprinting—bioprinting from benchside to bedside? Acta Biomater 101:14–25. https://doi.org/10.1016/j.actbio.2019.08.045

10. Albanna M, Binder KW, Murphy SV et al (2019) In situ bioprinting of autologous skin cells accelerates wound healing of extensive excisional full-thickness wounds. Sci Rep 9:1856. https://doi.org/10.1038/s41598-018-38366-w
11. Zhao WX, Chen HY, Zhang Y et al (2022) Adaptive multi-degree-of-freedom in situ bioprinting robot for hair-follicle-inclusive skin repair: a preliminary study conducted in mice. Bioeng Translat Med 7(3):e10303. https://doi.org/10.1002/btm2.10303
12. Di Bella C, Duchi S, O'Connell CD et al (2018) In situ handheld three-dimensional bioprinting for cartilage regeneration. J Tissue Eng Regen Med 12(3):611–621. https://doi.org/10.1002/term.2476
13. Moncal KK, Gudapati H, Godzik KP et al (2021) Intra-operative bioprinting of hard, soft, and hard/soft composite tissues for craniomaxillofacial reconstruction. Adv Funct Mater 31(29):2010858. https://doi.org/10.1002/adfm.202010858
14. Zhao WX, Hu CX, Xu T et al (2022) Subaqueous bioprinting: a novel strategy for fetal membrane repair with 7-axis robot-assisted minimally invasive surgery. Adv Funct Mater 32(51):2207496. https://doi.org/10.1002/adfm.202207496
15. Russell CS, Mostafavi A, Quint JP et al (2020) In situ printing of adhesive hydrogel scaffolds for the treatment of skeletal muscle injuries. ACS Appl Bio Mater 3(3):1568–1579. https://doi.org/10.1021/acsabm.9b01176
16. Alkadi F, Lee KC, Bashiri AH et al (2020) Conformal additive manufacturing using a direct-print process. Addit Manuf 32:100975. https://doi.org/10.1016/j.addma.2019.100975
17. Chen LF, Chung MF, Tian YB et al (2019) Variable-depth curved layer fused deposition modeling of thin-shells. Robot Comput Integr Manuf 57:422–434. https://doi.org/10.1016/j.rcim.2018.12.016
18. Nayyeri P, Zareinia K, Bougherara H (2022) Planar and nonplanar slicing algorithms for fused deposition modeling technology: a critical review. Int J Adv Manuf Technol 119(5-6):2785–2810. https://doi.org/10.1007/s00170-021-08347-x
19. Wang HC, Lian Q, Li DC et al (2021) Multi-tissue layering and path planning of in situ bioprinting for complex skin and soft tissue defects. Rapid Prototyping J 27(2):321–332. https://doi.org/10.1108/RPJ-08-2020-0201
20. Mitropoulou I, Bernhard M, Dillenburger B (2020) Print paths key-framing: design for non-planar layered robotic FDM printing. In: Proceedings of the 5th Annual ACM Symposium on Computational Fabrication, p.1–10. https://doi.org/10.1145/3424630.3425408
21. Mitropoulou I, Bernhard M, Dillenburger B (2022) Nonplanar 3D printing of bifurcating forms. 3D Print Addit Manuf 9(3):189–202. https://doi.org/10.1089/3dp.2021.0023
22. Fortunato GM, Nicoletta M, Batoni E et al (2023) A fully automatic non-planar slicing algorithm for the additive manufacturing of complex geometries. Addit Manuf 69:103541. https://doi.org/10.1016/j.addma.2023.103541
23. Yigit IE, Lazoglu I (2020) Spherical slicing method and its application on robotic additive manufacturing. Prog Addit Manuf 5(4): 387–394. https://doi.org/10.1007/s40964-020-00135-5
24. Yigit IE, Lazoglu I (2019) Helical slicing method for material extrusion-based robotic additive manufacturing. Prog Addit Manuf 4(3):225–232. https://doi.org/10.1007/s40964-019-00090-w
25. Yigit IE, Khan SA, Lazoglu I (2022) Robotic additive turning with a novel cylindrical slicing method. Int J Adv Manuf Technol 119(11-12):7641–7651. https://doi.org/10.1007/s00170-021-08567-1
26. Zou Q, Zhao JB (2013) Iso-parametric tool-path planning for point clouds. Comput Aided Des 45(11):1459–1468. https://doi.org/10.1016/j.cad.2013.07.001
27. Fortunato GM, Rossi G, Bonatti AF et al (2021) Robotic platform and path planning algorithm for in situ bioprinting. Bioprinting 22:e00139. https://doi.org/10.1016/j.bprint.2021.e00139
28. Fortunato GM, Batoni E, Bonatti AF et al (2022) Surface reconstruction and tissue recognition for robotic-based in situ bioprinting. Bioprinting 26:e00195. https://doi.org/10.1016/j.bprint.2022.e00195
29. Kucukdeger E, Tong YX, Singh M et al (2021) Conformal 3D printing of non-planar antennas on wrinkled and folded kapton films using point cloud data. Flex Print Electron 6(4):044002. https://doi.org/10.1088/2058-8585/ac28f1
30. Lian Q, Li X, Li DC et al (2019) Path planning method based on discontinuous grid partition algorithm of point cloud for in situ printing. Rapid Prototyp J 25(3):602–613. https://doi.org/10.1108/RPJ-03-2018-0056
31. Zhou C, Yang YZ, Wang JX et al (2021) Ferromagnetic soft catheter robots for minimally invasive bioprinting. Nat Commun 12(1):5072. https://doi.org/10.1038/s41467-021-25386-w
32. Rodriguez-Padilla C, Cuan-Urquizo E, Roman-Flores A et al (2021) Algorithm for the conformal 3D printing on non-planar tessellated surfaces: applicability in patterns and lattices. Appl Sci 11(16):7509. https://doi.org/10.3390/app11167509
33. Huang YA, Wu H, Zhu C et al (2021) Programmable robotized 'transfer-and-jet' printing for large, 3D curved electronics on complex surfaces. Int J Extr Manuf 3(4):045101. https://doi.org/10.1088/2631-7990/ac115a
34. Jafari BH, Gans N (2020) Surface parameterization and trajectory generation on regular surfaces with application in robot-guided deposition printing. IEEE Robot Autom Lett 5(4):6113–6120. https://doi.org/10.1109/LRA.2020.3010454
35. Weingartshofer T, Haddadi A, Hartl-Nesic C et al (2022) Flexible robotic drawing on 3D objects with an industrial robot. In: Proceedings of the 2022 IEEE Conference on Control Technology and Applications (CCTA): IEEE, p.29–36. https://doi.org/10.1109/CCTA49430.2022.9966015
36. Bomze IM, Demyanov VF, Fletcher R et al (2010) Interior point methods for nonlinear optimization. Lect Note Math 1989: 215–276. https://doi.org/10.1007/978-3-642-11339-0_4
37. Korenius T, Laurikkala J, Juhola M (2007) On principal component analysis, cosine and Euclidean measures in information retrieval. Inform Sci 177(22):4893–4905. https://doi.org/10.1016/j.ins.2007.05.027
38. Qian G, Sural S, Gu YL et al (2004) Similarity between Euclidean and cosine angle distance for nearest neighbor queries. In: Proceedings of the 2004 ACM Symposium on Applied Computing, p.1232–1237. https://doi.org/10.1145/967900.968151
39. Zhao DH, Guo WZ (2020) Shape and performance controlled advanced design for additive manufacturing: a review of slicing and path planning. J Manuf Sci Eng 142(1):010801. https://doi.org/10.1115/1.4045055
40. Ozler SB, Bakirci E, Kucukgul C et al (2017) Three-dimensional direct cell bioprinting for tissue engineering. J Biomed Mater Res Part B Appl Biomater 105(8):2530–2544. https://doi.org/10.1002/jbm.b.33768
41. Guo XY, Xiao J, Wang Y (2018) A survey on algorithms of hole filling in 3D surface reconstruction. Vis Comput 34(1):93–103. https://doi.org/10.1007/s00371-016-1316-y
42. Vedaldi A, Fulkerson B (2010) VLFeat: an open and portable

library of computer vision algorithms. In: Proceedings of the 18th ACM International Conference on Multimedia, p.1469–1472. https://doi.org/10.1145/1873951.1874249
43. Zhao WX, Hu CX, Lin SZ et al (2023) A closed-loop minimally invasive 3D printing strategy with robust trocar identification and adaptive alignment. Addit Manuf 73:103701. https://doi.org/10.1016/j.addma.2023.103701
44. Chen MH, Wang LL, Chung JJ et al (2017) Methods to assess shear-thinning hydrogels for application as injectable biomaterials. ACS Biomater Sci Eng 3(12):3146–3160. https://doi.org/10.1021/acsbiomaterials.7b00734
45. Olofsson B (2015) Topics in machining with industrial robot manipulators and optimal motion control. PhD Thesis of Lund University.
46. Shembekar AV, Yoon YJ, Kanyuck A et al (2019) Generating robot trajectories for conformal three-dimensional printing using nonplanar layers. J Comput Inform Sci Eng 19(3):031011. https://doi.org/10.1115/1.4043013
47. Weiss V, Andor L, Renner G et al (2002) Advanced surface fitting techniques. Comput Aided Geom Des 19(1):19–42. https://doi.org/10.1016/S0167-8396(01)00086-3
48. Pratt V (1987) Direct least-squares fitting of algebraic surfaces. ACM SIGGRAPH Comput Graph 21(4):145–152. https://doi.org/10.1145/37402.37420
49. Wang J, Yu ZY (2011) Quadratic curve and surface fitting via squared distance minimization. Comput Graph 35(6):1035–1050. https://doi.org/10.1016/j.cag.2011.09.001
50. Huang YA, Wu H, Xiao L et al (2019) Assembly and applications of 3D conformal electronics on curvilinear surfaces. Mater Horiz 6(4):642–683. https://doi.org/10.1039/c8mh01450g
51. Adams JJ, Duoss EB, Malkowski TF et al (2011) Conformal printing of electrically small antennas on three-dimensional surfaces. Adv Mater 23(11):1335–1340. https://doi.org/10.1002/adma.201003734
52. Ding HZ, Chang RC (2018) Simulating image-guided in situ bioprinting of a skin graft onto a phantom burn wound bed. Addit Manuf 22:708–719. https://doi.org/10.1016/j.addma.2018.06.022
53. Fu ZQ, Naghieh S, Xu CC et al (2021) Printability in extrusion bioprinting. Biofabrication 13(3):033001. https://doi.org/10.1088/1758-5090/abe7ab
54. Fortunato GM, Batoni E, Pasqua L et al (2023) Automatic photo-cross-linking system for robotic-based in situ bioprinting. ACS Biomater Sci Eng 9(12):6926–6934. https://doi.org/10.1021/acsbiomaterials.3c00898